Sensor noise in LISA Pathfinder: Laser frequency noise and its coupling to the optical test mass readout

Journal Article

Author(s):
Armano, Michele; Audley, H.; Baird, J.; Born, Max; Bortoluzzi, D.; Brandt, N.; Castelli, Edoardo; Cavalleri, A.; Cesarini, A.; Cruise, Adrian Michael; Danzmann, Karsten; de Deus Silva, M.; Diepholz, Ingo; Dixon, G.; Dolesi, Rita; Ferraioli, Luigi; Ferroni, Valerio; Fitzsimons, Ewan D.; Flatscher, R.; Giardini, Domenico; Mance, D.; Meshksar, Neda; Zweifel, P.; et al.

Sensor noise in *LISA Pathfinder*: Laser frequency noise and its coupling to the optical test mass readout

M. Armano,[1] H. Audley,[2,3] J. Baird,[4] P. Binetruy,[4,*] M. Born,[2,3] D. Bortoluzzi,[5] N. Brandt,[6] E. Castelli,[7] A. Cavalleri,[8] A. Cesarini,[9] A. M. Cruise,[10] K. Danzmann,[2,3] M. de Deus Silva,[11] I. Diepholz,[2,3] G. Dixon,[10] R. Dolesi,[7] L. Ferraioli,[12] V. Ferroni,[7] E. D. Fitzsimons,[13] R. Flatscher,[6] M. Freschi,[11] A. García,[14] R. Gerndt,[6] L. Gesa,[15,16,†] D. Giardini,[12] F. Gibert,[7,17] R. Giusteri,[2,3] C. Grimani,[9] J. Grzymisch,[1] F. Guzman,[18] I. Harrison,[19] M.-S. Hartig,[2,3] G. Hechenblaikner,[6] G. Heinzel,[2,3] M. Hewitson,[2,3] D. Hollington,[20] D. Hoyland,[10] M. Hueller,[7] H. Inchauspé,[4,§] O. Jennrich,[1] P. Jetzer,[21] U. Johann,[6] B. Johlander,[1] N. Karnesis,[4] B. Kaune,[2,3] C. J. Killow,[22] N. Korsakova,[4] J. A. Lobo,[15,16,‡] J. P. López-Zaragoza,[15] R. Maarschalkerweerd,[19] D. Mance,[12] V. Martín,[15,16] L. Martin-Polo,[11] F. Martin-Porqueras,[11] J. Martino,[4] P. W. McNamara,[1] J. Mendes,[19] L. Mendes,[11] N. Meshksar,[12] A. Monsky,[23] M. Nofrarias,[15] S. Paczkowski[●],[2,3,‖] M. Perreur-Lloyd,[22] A. Petiteau,[4] E. Plagnol,[4] J. Ramos-Castro,[24] J. Reiche,[2,3] F. Rivas,[25] D. I. Robertson,[22] G. Russano,[7,¶] J. Sanjuan,[26] J. Slutsky,[27] C. F. Sopuerta,[15] F. Steier,[23] T. Sumner,[20,26] D. Texier,[11] J. I. Thorpe,[27] D. Vetrugno,[7] S. Vitale,[7] V. Wand,[23] G. Wanner,[3,2] H. Ward,[22] P. J. Wass,[20,28] W. J. Weber,[7] L. Wissel,[2,3] A. Wittchen,[2,3] and P. Zweifel[12]

[1]*European Space Technology Centre, European Space Agency,*
Keplerlaan 1, 2200 AG Noordwijk, The Netherlands
[2]*Max Planck Institute for Gravitational Physics (Albert-Einstein-Institut), 30167 Hannover, Germany*
[3]*Leibniz Universität Hannover, 30167 Hannover, Germany*
[4]*Université Paris Cité, CNRS, Astroparticule et Cosmologie, F-75013 Paris, France*
[5]*Department of Industrial Engineering, University of Trento, via Sommarive 9, 38123 Trento, and Trento*
Institute for Fundamental Physics and Application/INFN
[6]*Airbus Defence and Space, Claude-Dornier-Strasse, 88090 Immenstaad, Germany*
[7]*Dipartimento di Fisica, Università di Trento and Trento Institute for Fundamental Physics*
and Application/INFN, 38123 Povo, Trento, Italy
[8]*Istituto di Fotonica e Nanotecnologie, CNR-Fondazione Bruno Kessler, I-38123 Povo, Trento, Italy*
[9]*DISPEA, Università di Urbino Carlo Bo, Via S. Chiara, 27 61029 Urbino/INFN, Italy*
[10]*The School of Physics and Astronomy, University of Birmingham, Birmingham, United Kingdom*
[11]*European Space Astronomy Centre, European Space Agency,*
Villanueva de la Cañada, 28692 Madrid, Spain
[12]*Institut für Geophysik, ETH Zürich, Sonneggstrasse 5, CH-8092, Zürich, Switzerland*
[13]*The UK Astronomy Technology Centre, Royal Observatory,*
Edinburgh, Blackford Hill, Edinburgh EH9 3HJ, United Kingdom
[14]*City University of Applied Sciences, Flughafenallee 10, 28199 Bremen, Germany*
[15]*Institut de Ciències de l'Espai (ICE, CSIC),*
Campus UAB, Carrer de Can Magrans s/n, 08193 Cerdanyola del Vallès, Spain
[16]*Institut d'Estudis Espacials de Catalunya (IEEC),*
C/ Gran Capità 2-4, 08034 Barcelona, Spain
[17]*isardSAT SL, Marie Curie 8-14, 08042 Barcelona, Catalonia, Spain*
[18]*Texas A&M University, 701 H.R. Bright Bldg, College Station, Texas 77843-3141, USA*
[19]*European Space Operations Centre, European Space Agency, 64293 Darmstadt, Germany*
[20]*High Energy Physics Group, Physics Department, Imperial College London, Blackett Laboratory,*
Prince Consort Road, London SW7 2BW, United Kingdom
[21]*Physik Institut, Universität Zürich, Winterthurerstrasse 190, CH-8057 Zürich, Switzerland*
[22]*SUPA, Institute for Gravitational Research, School of Physics and Astronomy, University of Glasgow,*
Glasgow G12 8QQ, United Kingdom
[23]*OHB System AG, Universitätsallee 27-29, 28359 Bremen, Germany*
[24]*Department d'Enginyeria Electrònica, Universitat Politècnica de Catalunya, 08034 Barcelona, Spain*
[25]*Universidad Loyola, Departament of Quantitative Methods,*
Avenida de las Universidades s/n, 41704 Dos Hermanas, Sevilla, Spain
[26]*Department of Physics, 2001 Museum Road, University of Florida, Gainesville, Florida 32611, USA*
[27]*Gravitational Astrophysics Lab, NASA Goddard Space Flight Center,*
8800 Greenbelt Road, Greenbelt, Maryland 20771, USA

[28]*Department of Mechanical and Aerospace Engineering, MAE-A, P.O. Box 116250, University of Florida, Gainesville, Florida 32611, USA*

The *LISA Pathfinder* (LPF) mission successfully demonstrated the feasibility of the technology needed for the future space borne gravitational wave observatory LISA. A key subsystem under study was the laser interferometer, which measured the changes in relative distance in between two test masses (TMs). It achieved a sensitivity of $32.0^{+2.4}_{-1.7}$ fm/$\sqrt{\text{Hz}}$, which was significantly better than the prelaunch tests. This improved performance allowed direct observation of the influence of laser frequency noise in the readout. The differences in optical path lengths between the measurement and reference beams in the individual interferometers of our setup determined the level of this undesired readout noise. Here, we discuss the dedicated experiments performed on LPF to measure these differences with high precision. We reached differences in path length difference between (368 ± 5) μm and (329.6 ± 0.9) μm which are significantly below the required level of 1 mm or 1000 μm. These results are an important contribution to our understanding of the overall sensor performance. Moreover, we observed varying levels of laser frequency noise over the course of the mission. We provide evidence that these do not originate from the laser frequency stabilization scheme which worked as expected. Therefore, this frequency stabilization would be applicable to other missions with similar laser frequency stability requirements.

I. INTRODUCTION

The LPF mission successfully demonstrated the feasibility of the technology needed for the future space-borne gravitational wave observatory Laser Interferometer Space Antenna (LISA) [1–3]. It was an ESA-led satellite mission launched on December 3, 2015, and shut down on July 18, 2017. More precisely, the main aim of the mission was to experimentally show that two TMs in a satellite can be in free-fall as needed for LISA. With LPF, we found that the undesired residual differential acceleration between these two TMs could be limited to (1.74 ± 0.05) fm/s$^2\sqrt{\text{Hz}}$ above 2 mHz [4,5].

To achieve the LPF free-fall performance, a high-precision readout of the changes in the distance between two TMs was needed. Therefore, a heterodyne laser interferometry setup was used. It achieved a sensitivity of $32.0^{+2.4}_{-1.7}$ fm/$\sqrt{\text{Hz}}$ above 200 mHz, which was mainly limited by phasemeter

*Deceased 30 March 2017
†Deceased 29 May 2020
‡Deceased 30 September 2012
§Present address: Institut für Theoretische Physik, Universität Heidelberg, Philosophenweg 16, 69120 Heidelberg, Germany.
‖sarah.paczkowski@aei.mpg.de
¶Present address: INAF Osservatorio Astronomico di Capodimonte, I-80131 Napoli, Italy.

readout noise and laser frequency noise [6,7]. Consequently, the measurements and results presented here deepen the understanding of laser frequency fluctuations and their couplings to the relative displacement measurement, and thus provide an important contribution to the modeling and understanding of the sensor performance.

When an interferometer measures a change in distance, this means that the optical path length difference (OPD) between its measurement and the reference beam, Δs, is changed. The corresponding measured phase, $\Delta \varphi$, is then given by

$$\Delta \varphi = \frac{2\pi}{\lambda} \Delta s \qquad (1)$$

with λ being the wavelength of the laser light. Using $\lambda = \frac{c}{f}$, with c as the speed of light, we can write Eq. (1) as

$$\Delta \varphi = \frac{2\pi}{c} \Delta s f. \qquad (2)$$

Hence, laser frequency fluctuations $\delta \tilde{f}$ cause fluctuations in the measured phase $\Delta \tilde{\varphi}$ [8,9]:

$$\Delta \tilde{\varphi} = \frac{2\pi}{c} \Delta s \delta \tilde{f}. \qquad (3)$$

These fluctuations are, by principle, indistinguishable from a true motion. Equation (3) is of key importance for this paper. From this equation, we can see that the undesired phase fluctuations are proportional to the OPD Δs and the

laser frequency fluctuations $\delta\tilde{f}$. Accordingly, these two quantities were minimized by design. In the following, we will show experimental results relating to the OPDs Δs and the laser frequency fluctuations $\delta\tilde{f}$ during the LPF mission.

Overall, this undesired phase noise was successfully suppressed. We reached differences in optical path length difference (DOPDs) between (368 ± 5) µm and (329.6 ± 0.8) µm which are significantly below the required level of 1 mm or 1000 µm. Similar to Δs in Eq. (3), these values determine the coupling of laser frequency noise into the readout of the distance changes in between the two TMs on LPF. Moreover, we provide evidence that the laser frequency stabilization worked as expected to suppress $\delta\tilde{f}$ and would, therefore, be applicable to other missions with similar laser frequency stability requirements.

This paper is outlined as follows: first, we summarize a few relevant facts about the laser interferometry setup in Sec. II. Then, we rewrite Eq. (3) for the case of the available telemetry from LPF and introduce the DOPD in Sec. III. During LPF operations, we performed dedicated experiments to measure the coupling factor from laser frequency fluctuations into the TM position readout, the DOPD. These experiments relied on modulations of the laser frequency. The details are explained in Sec. IV, where we derive the results used in [6,7]. Moreover, since this factor depends on the absolute TM positions, it provides a means to measure these. We discuss the characterization of the laser frequency stabilization in Sec. V. This also includes in-loop measurements of the laser frequency noise. We summarize the path length matching achieved and the advantages and disadvantages of this laser frequency stabilization scheme in Sec. VI.

II. THE LISA PATHFINDER OPTICAL METROLOGY SYSTEM

The laser interferometric optical readout of the position and orientation of both TMs was called the optical metrology system (OMS). It was designed to operate at a noise level of a few pm/$\sqrt{\text{Hz}}$ and nrad/$\sqrt{\text{Hz}}$. The OMS performed heterodyne interferometry at a frequency of 1 kHz in-flight [6,7,10–12].

In Fig. 1, we schematically illustrate the units involved in the proper functioning of the OMS. The reference laser unit contained a single Nd:YAG nonplanar ring oscillator with a wavelength of 1064 nm. The nominal output power from the laser crystal was approximately 35 mW. The light was transmitted via optical fibers to the laser modulator unit, where it was split into two beams, which were each frequency shifted by an acousto-optic modulator. Each of the two beams was guided through a fiber to the optical bench (OB).

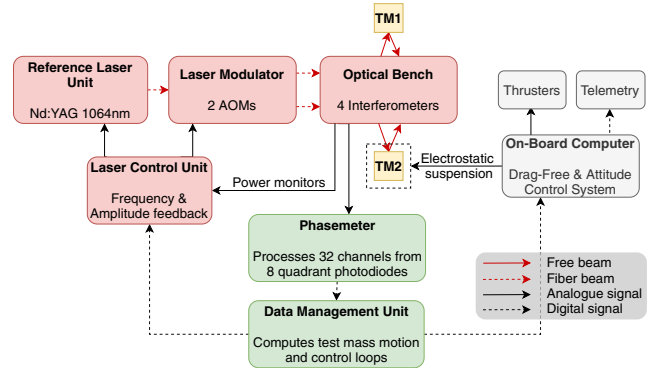The ultrastable OB hosted four Mach-Zehnder-style interferometers, as drawn in the upper panel of Fig. 2.

FIG. 1. Overview of the main components of the LPF OMS. This paper will look at the frequency stabilization of the reference laser unit (on the left) and the interferometer path length differences on the OB (in the center). The laser frequency controller, which we will characterize in Sec. V is inside the DMU. The actuators are inside the laser control unit. Reprint from [7] for convenience.

One of these four was the so-called X1 interferometer, which measured the position and rotational orientation of TM 1 with respect to the OB and so essentially to the satellite. Additionally, the X12 interferometer measured the changes in relative distance Δx in between the two TMs as well as the differential orientation. The orientations were measured via a technique called differential wavefront sensing (DWS) [13]. The other two interferometers are auxiliary and were used to ensure the necessary precision of the OMS X1 and X12 readouts. One of them was the reference interferometer XR, which measured the common mode path length fluctuations that occurred in the fibers before the light reached the OB. In addition, there was the frequency interferometer XF with an intentional OPD Δs of 38.2 cm, with an uncertainty on the millimeter level, to increase the coupling of the laser frequency fluctuations, it was designed to measure [14]. It is shown in the lower panel of Fig. 2. This interferometer was a key part of the laser frequency stabilization scheme on LPF, which we will describe in more detail in Sec. III and analyze its in-flight performance in Sec. V.

Each interferometer measurement was simultaneously recorded by two photodiodes at the two Mach-Zehnder outputs in a redundant balanced detection scheme. To be more specific, these photodiodes were quadrant photodiodes which was essential for the DWS measurements. These beat note signals were then used by the phasemeter (green box in Fig. 1) to extract, among other quantities, a longitudinal phase for each of the four interferometers. We call these phases x_1, x_{12}, x_R and x_F. In the next step, the reference interferometer phase x_R was subtracted from each of the other three phases in the data management unit (DMU). In addition, for the two measurements of changes in the TMs positions, we applied a scaling factor from
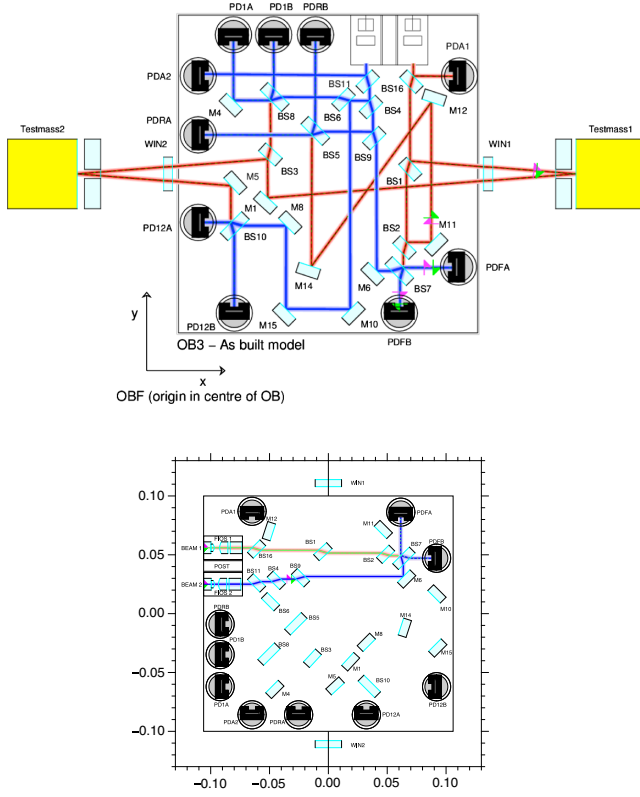
FIG. 2. Upper panel: The four interferometers on the OB. Lower panel: The frequency interferometer XF measured the laser frequency fluctuations. Note that the coordinate systems in the upper and lower panels are rotated with respect to each other by 90°. Reprint from [7] for convenience.

phase to distance. After the subtraction and scaling, we obtained the following measurements [7]:

$$o_1 = \frac{1}{2}\frac{\lambda}{2\pi}\frac{1}{\cos(\alpha)} \cdot (x_1 - x_R)$$

$$o_{12} = -\frac{1}{2}\frac{\lambda}{2\pi}\frac{1}{\cos(\alpha)} \cdot (x_{12} - x_R)$$

$$\Psi_R = x_R$$

$$\Psi_F = x_F - x_R \tag{4}$$

Here, we have a factor $\frac{1}{2}$ to account for the fact that the light travels to the TM and back. λ denotes the laser wavelength and accordingly, the factor $\frac{\lambda}{2\pi}$ converts our phase measurement in radians to a distance measurement in meters. The division by $\cos(\alpha)$ is the result of the laser beam hitting the TMs under an angle of $\alpha = 4.5°$.

The DMU used the Ψ_R and Ψ_F measurements in a control loop to minimize the OPD, see, e.g., [7], and in the control loop for laser frequency stabilization. We will give more details on the latter in Sec. III. In the case of the laser frequency stabilization control loop, the calculated actuation signal was then fed from the DMU to the laser control unit. The onboard computer also processed data from the

DMU. The drag-free and attitude control system of the satellite used the o_{12} and o_1 measurements to determine the necessary electrostatic force actuation on the TM and μN cold gas thrust on the SC, respectively [4,15,16]. As an alternative to the o_{12} and o_1 measurements, the positions of the two TMs could be measured electrostatically, too [17]. This was also how we measured the degrees of freedom inaccessible to the interferometry. Moreover, the onboard computer also provided the telemetry, part of which are the four measurements of Eq. (4). We will use these for the analysis of Secs. IV and V.

III. LASER FREQUENCY NOISE IN THE OMS

The laser was stabilized using a nested control loop to minimize the amount of laser frequency noise. It is shown schematically in Fig. 3. The processed frequency inter-ferometer measurement Ψ_F was fed into the fast frequency controller (C_F) inside the DMU. It determined the neces-sary voltage applied by a piezo-electric transducer (A_F) on the laser crystal. The fast frequency controller output was further processed by a slow frequency controller (C_S), which determined the necessary voltage applied to the slow frequency actuator (A_S) which was a laser crystal heater. For more details, we refer to [18]. We will discuss the performance of this loop in-flight in Sec. V.

Let us now proceed to look at Eq. (3) in terms of the available telemetry as defined by Eq. (4), as also developed in [19]. We begin with writing Eq. (3) for each of the four interferometers:

$$\Delta\tilde{\varphi}_{X1} = \frac{2\pi}{c}\Delta s_{X1}\delta\tilde{f}, \tag{5}$$

$$\Delta\tilde{\varphi}_{X12} = \frac{2\pi}{c}\Delta s_{X12}\delta\tilde{f}, \tag{6}$$
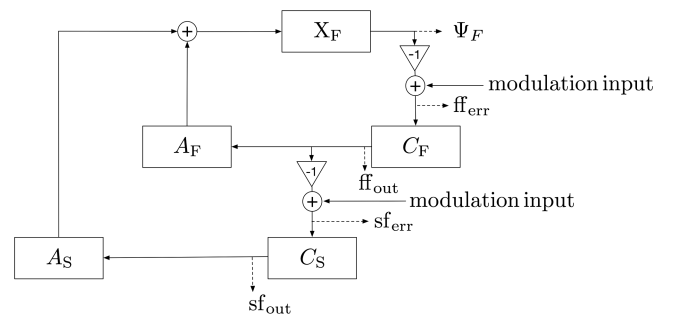

FIG. 3. The control loop used on LPF to stabilize the laser frequency. The frequency interferometer XF measured the laser frequency fluctuations. The processed measurement available on-ground is denoted Ψ_F. The modulation input in front of the fast frequency controller C_F was used for the experiments discussed in Secs. IV and V. The loop components are explained in the text. Reprint from [19].

$$\Delta\tilde{\varphi}_{\mathrm{XR}} = \frac{2\pi}{c}\Delta s_{\mathrm{XR}}\delta\tilde{f}, \tag{7}$$

$$\Delta\tilde{\varphi}_{\mathrm{XF}} = \frac{2\pi}{c}\Delta s_{\mathrm{XF}}\delta\tilde{f}. \tag{8}$$

We can then divide each of these OPDs into a common OPD occurring in the fibers before the light enters the OB and a second part on the OB. Then, Eqs. (5)–(8) read:

$$\Delta\tilde{\varphi}_{\mathrm{X1}} = \frac{2\pi}{c}(\Delta s_{\mathrm{fiber}} + \Delta s_{\mathrm{X1\,on\,OB}})\delta\tilde{f} \tag{9}$$

$$\Delta\tilde{\varphi}_{\mathrm{X12}} = \frac{2\pi}{c}(\Delta s_{\mathrm{fiber}} + \Delta s_{\mathrm{X12\,on\,OB}})\delta\tilde{f} \tag{10}$$

$$\Delta\tilde{\varphi}_{\mathrm{XR}} = \frac{2\pi}{c}(\Delta s_{\mathrm{fiber}} + \Delta s_{\mathrm{XR\,on\,OB}})\delta\tilde{f} \tag{11}$$

$$\Delta\tilde{\varphi}_{\mathrm{XF}} = \frac{2\pi}{c}(\Delta s_{\mathrm{fiber}} + \Delta s_{\mathrm{XF\,on\,OB}})\delta\tilde{f} \tag{12}$$

The available telemetry as given by Eq. (4) is subject to more processing steps. If we take the subtraction of x_{R} and the scaling to a change in position into account, we obtain for the contribution of laser frequency noise $\delta\tilde{f}$ to the phase noise in the differential TM readout

$$\tilde{o}_{12} = -\frac{\lambda}{4\pi\cos(\alpha)}\left(\frac{2\pi}{c}(\Delta s_{\mathrm{fiber}} + \Delta s_{\mathrm{X12\,on\,OB}})\right.$$
$$\left. - \frac{2\pi}{c}(\Delta s_{\mathrm{fiber}} + \Delta s_{\mathrm{XR\,on\,OB}})\right)\delta\tilde{f}, \tag{13}$$

which simplifies to

$$\tilde{o}_{12} = -\frac{\lambda}{4\pi\cos(\alpha)}\frac{2\pi}{c}(\Delta s_{\mathrm{X12\,on\,OB}} - \Delta s_{\mathrm{XR\,on\,OB}})\delta\tilde{f}, \tag{14}$$

because the common mode path length differences occurring in the fibers, $\Delta s_{\mathrm{fiber}}$, drop out due to the subtraction of the reference interferometer measurement. Similarly, we find for the frequency interferometer telemetry

$$\tilde{\Psi}_{\mathrm{F}} = \frac{2\pi}{c}(\Delta s_{\mathrm{XF\,on\,OB}} - \Delta s_{\mathrm{XR\,on\,OB}})\delta\tilde{f}. \tag{15}$$

However, on LPF we measured the laser frequency fluctuations via the phase of the frequency interferometer. There was no additional, independent sensor on the LPF satellite. Accordingly, we have to solve Eq. (15) for $\delta\tilde{f}$ and insert into Eq. (14). Let us note explicitly that this insertion is based on two reasonable assumptions. First, that *all* the noise measured in the frequency interferometer is due to laser frequency noise, and second, that this measurement is indeed the *instantaneous* contribution of laser frequency noise to the o_{12} readout. We then obtain:

$$\tilde{o}_{12} = -\frac{\lambda}{4\pi\cos(\alpha)}\frac{\Delta s_{\mathrm{X12\,on\,OB}} - \Delta s_{\mathrm{XR\,on\,OB}}}{\Delta s_{\mathrm{XF\,on\,OB}} - \Delta s_{\mathrm{XR\,on\,OB}}}\tilde{\Psi}_{\mathrm{F}}. \tag{16}$$

This equation also holds if we calculate the square root of the power spectral densities (PSDs) of the o_{12} and Ψ_{F} measurements:

$$S_{o_{12},\mathrm{freq}}^{1/2} = -\frac{\lambda}{4\pi\cos(\alpha)}\frac{\Delta s_{\mathrm{X12\,on\,OB}} - \Delta s_{\mathrm{XR\,on\,OB}}}{\Delta s_{\mathrm{XF\,on\,OB}} - \Delta s_{\mathrm{XR\,on\,OB}}}S_{\Psi_{\mathrm{F}}}^{1/2}, \tag{17}$$

which is similar to Eq. (3) in [6]. Let us examine Eq. (16). The denominator $\Delta s_{\mathrm{XF\,on\,OB}} - \Delta s_{\mathrm{XR\,on\,OB}}$ is the DOPD between the frequency and reference interferometer on the OB. To understand this term, it is important to know that the OPD between the measurement and the reference beam was introduced by different lengths of the two fibers, which brought the light to the OB. The XR interferometer was then built in such a way that the path of the beams on the OB differed to compensate for the OPD occurring in the fibers. For the XF interferometer, the paths on the OB itself were matched to within construction limits since the OPD in the fibers amplified the frequency fluctuations which it was designed to measure. Accordingly, $\Delta s_{\mathrm{XF\,on\,OB}} - \Delta s_{\mathrm{XR\,on\,OB}}$ was dominated by $\Delta s_{\mathrm{XR\,on\,OB}}$ which amounted to 38.2 cm[1] with an uncertainty on the millimeter level [14]. Different to the X1 and X12 interferometers, both beams of the XF and XR interferometer were routed on the OB. Since the OB with all its components is ultrastable, we can assume that this value did not change between manufacturing and the mission, and we can use the construction value. We then define

$$\Delta s_{o12} = \Delta s_{\mathrm{X12\,on\,OB}} - \Delta s_{\mathrm{XR\,on\,OB}}, \tag{18}$$

which determines the nominator of Eq. (16). It is the DOPD of the X12 and the reference interferometer. Analogously, we define Δs_{o1} as the DOPD of the X1 and the reference interferometer. We can then write Eq. (16) as

$$\tilde{o}_{12} = -\frac{\lambda}{4\pi\cos(\alpha)}\frac{\Delta s_{o12}}{\Delta s_{\mathrm{XF\,on\,OB}} - \Delta s_{\mathrm{XR\,on\,OB}}}\tilde{\Psi}_{\mathrm{F}}. \tag{19}$$

Δs_{o12} depends not only on the construction tolerances but also on the precise positions of the two TMs. These absolute positions of the TMs with respect to the OB are a result of the commanded offsets and the satellite's core assembling process because each piece of equipment was aligned with respect to the previous. In practice, that meant roughly aligning the OB to the side slabs, the side slabs to

---

[1]In Ref. [20], this value was denoted as 38.4 cm but the 38.2 cm are correct. In any case, the values are close enough so that there is no effect on the results of this paper, that is, the estimated DOPDs and measured frequency fluctuations agree to within the estimated uncertainties.
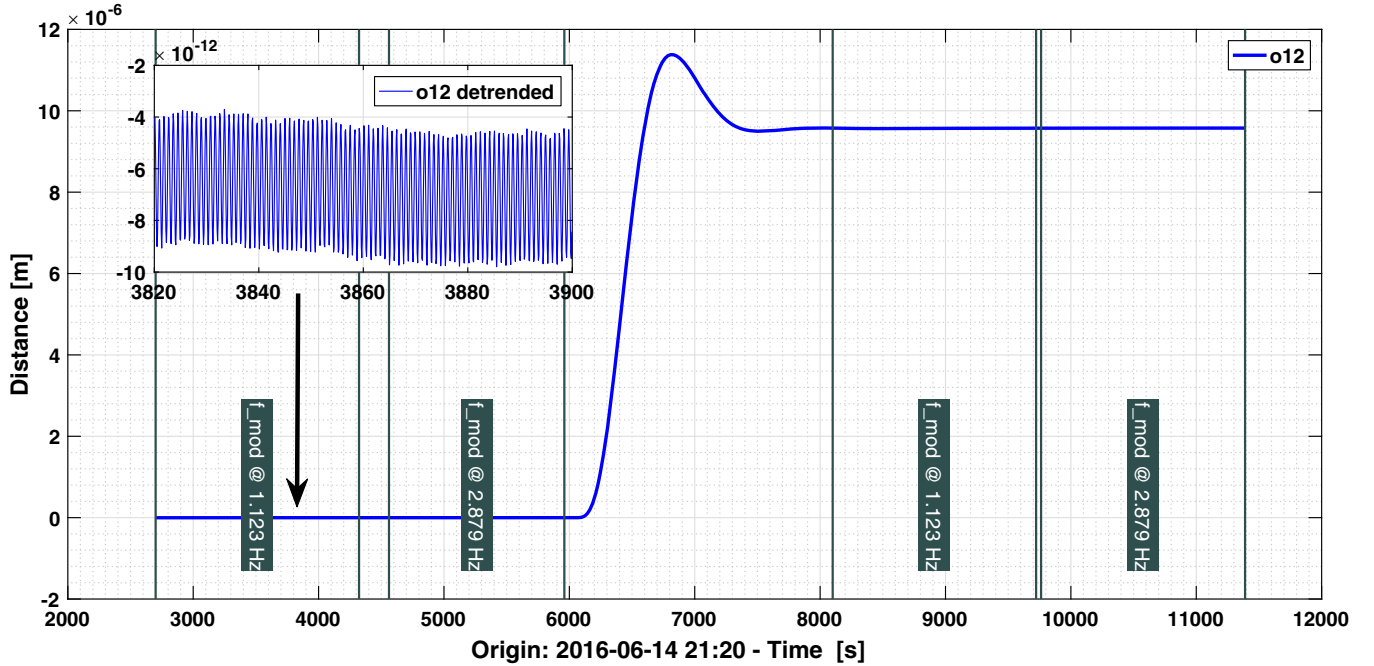
FIG. 4.   The concept of the DOPD offset experiment. At the nominal TM positions, the laser frequency was modulated two times, once at 1.123 Hz and once at 2.879 Hz. These modulations are discernible in the differential test mass readout o_{12} as shown, for example, in the inset figure. Then, a TM was moved to an offset position, which is visible by the change in the measured o_{12} value. Next, we repeated the laser frequency modulations. Reprint from [19].

the vacuum tanks, and the actuation and sensing electrodes around the TMs to the vacuum tanks before placing the TMs.

Early in the LPF development, the laser frequency requirement was set under the conservative assumption of a DOPD of $\Delta s_{o12} \leq 1$ cm [21]. A preflight ground measurement campaign placed an experimental upper limit of 400 μm on the DOPD [20], though this was not fully representative, with the TM replaced by mirrors at the nominal calculated TM positions.

Let us proceed with explaining the dedicated experiments performed in-flight with LPF to characterize the laser frequency stabilization and to estimate Δs_{o12}.

The key idea of all these experiments was to modulate the laser frequency. Therefore, we injected a sinusoidal test signal with a given amplitude and frequency into the modulation input in front of the fast frequency controller C_F (see Fig. 3). The experiments contained a different number of these test signals, which had varying amplitudes, frequencies, and durations. We designed and analyzed the experiments using the LISA technology package data analysis (LTPDA) [22].

IV. EXPERIMENTAL DOPD RESULTS

A. Description of experiments optimized for DOPD estimation

We successfully performed two experiments optimized to estimate the DOPD.

One of these was the DOPD offset experiment. It included two laser frequency modulations at the nominal TM position, from which we estimated the DOPD. Then, one of the TMs was shifted to an offset position, and we repeated the laser frequency modulations to estimate the DOPD. Figure 4 illustrates the concept of this experiment. It was successfully executed from 2016-06-14 at 21:30 until 2016-06-15 at 06:42:00 UTC. The change in DOPD should agree to the commanded offset, both in amplitude and direction.

Second, the DOPD amplitude experiment aimed to ensure that our measured DOPD is independent of the laser frequency modulation amplitude. We determined the DOPD using three different modulation amplitudes in this experiment. The experiment contained a total of four modulation segments. The second and the fourth modulation segments shared the same modulation amplitude but were performed at a different frequency (1.123 Hz vs. 2.879 Hz). These different frequencies allowed us to double-check that the estimated DOPD was independent of the modulation frequency, at least within this range. We executed the experiment on LPF from 2017-01-22 12:05 UTC to 2017-01-22 14:59 UTC, more than seven months after the DOPD offset experiment.

Moreover, we can also use data from the experiments optimized for the control loop characterization to estimate the DOPD. In total, we executed five of these experiments during the mission operations. Each of these five experiments contained several laser frequency modulations,

as will be described in more detail in Sec. V. However, for a valid comparison, we can only consider those experiments here that took place under the same conditions on the satellite as the dedicated DOPD experiments: the two TMs must have been free-falling, and the satellite control must have been configured for science measurements, cf. [4]. This criterion implies we can use the data from three of the five experiments optimized for the frequency loop characterization.

B. Analysis

To determine the DOPD, we solve Eq. (19) for Δs_{o12}. This means essentially comparing the amplitude of the injected sine wave in the XF interferometer, as measured by Ψ_F, to the resulting amplitude of the sine wave in o_{12} or o_1.

There are several approaches to comparing the signal amplitudes; see, for example, Sec. 5.2 in [19]. Here, we use the "DFT method" and the "TFE method." Most of the results shown here were obtained using the DFT method, which works like this: We divided the absolute values of the discrete Fourier transform of the two channels multiplied with a Blackman-Harris window at the modulation frequencies by one another. We then obtained an estimate of the error from the discrete Fourier transform of the respective channel at frequencies around the modulation frequency and then propagated the two estimated uncertainties through the division. We call this the DFT method, even though it comprises not only the calculation of the discrete Fourier transform. The TFE method computed a transfer function estimate as the ratio of the cross-power spectral density between the input and output to the power spectral density of the input [23,24]. We then took the absolute value of this transfer function at the modulation frequency to obtain a DOPD estimate. This procedure estimated the uncertainty from the coherence between the two signals. This method was applied to the DOPD offset experiment.

When we apply the DFT method to each laser frequency modulation segment, we obtain four DOPDs estimates in case of the DOPD offset experiment. Similarly, we estimate four DOPDs for the DOPD amplitude experiment. To find out how the DOPD changed over time, we calculated the weighted mean over all the modulations of one experiment and then collected the results in chronological order.

The DFT method was used to estimate both Δs_{o12} and Δs_{o1}. However, due to the increased noise in o_1 compared to o_{12}, see Fig. 4 in [7], there was often no signal from the frequency modulations in o_1 and so we could determine Δs_{o1} only for two experiments. We checked that the impact of the satellite control was negligible for both o_{12} and o_1 to within the errors. In the case of o_{12}, the reason is that the unity gain frequency of the respective satellite control loop is around 1 mHz [4] and thus below even our lowest laser frequency modulation frequency of 11 mHz. Nonetheless, we checked this via a dedicated simulation. Also, for o_1, there was a difference in frequency between the bandwidth

of the respective control loop and the laser modulation frequencies. In this case, the bandwidth of the control loop was around 250 mHz and the laser was frequency modulated at 1.123 Hz and 2.879 Hz in the experiments during which we could determine Δs_{o1}. Again, we performed a dedicated simulation, but any possible correction was deemed negligible given that it is on the order of magnitude of the uncertainty.

C. Results

We summarize the results from the DOPD offset experiment in Fig. 5. For each of the four modulations, we applied both the DFT method (blue dots) and the TFE method (black dots). We note that the results from the two methods agree with each other at roughly the 3σ level. The large uncertainties reported by the DFT method at the offset position are due to the increase in the noise floor of o_{12} at the offset position.

When designing the experiment, we expected the first two DOPD estimates to be identical on the µm level. We anticipated the same agreement for the third and fourth estimates but commonly offset as commanded. However, the true DOPD at both the starting and the offset position is unknown; only the commanded offset Δx is well known. We can write this in a simple model as

$$\text{DOPD}_{\text{offset}} = \Delta x + \text{DOPD}_{\text{nominal}}. \tag{20}$$

Then, we obtain a value for $\text{DOPD}_{\text{nominal}}$ from a weighted linear least-squares fit to the four DOPD estimates obtained via the TFE method. The result is shown in Fig. 5 in green. The standard deviation of this fit result is estimated to be below 1 µm and is therefore indiscernible in Fig. 5.
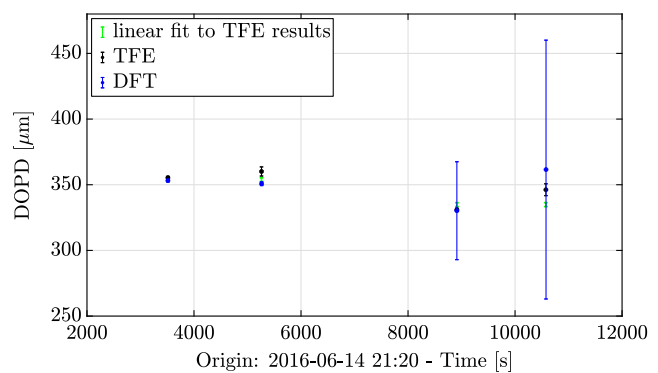

FIG. 5. Results of the DOPD offset experiment. The DOPD estimates from the TFE method are (355 ± 1) µm, (360 ± 3) µm, (330 ± 1) µm and (346 ± 4) µm (for modulations 1–4, respectively). The results from the two methods agree with each other at roughly the 3σ level. We find the same level of agreement between the "TFE results" and the model (shown in green). Therefore, we can associate the change in DOPD to the commanded offset, both in direction and amplitude, at this level. Based on [19].

When we fit the model of Eq. (20) to the TFE results, we find a match at the 3σ level, so we can associate the change in measured DOPD to the commanded offset at this level. The fit is not closer to the data because the model assumes one single nominal position for the first two modulations and another common offset position for the third and fourth modulation. When TM 2 was moved to a 9.576 µm offset position toward the center of the satellite, the path of the measurement beam was shortened (see Fig. 2). The electrostatic measurement system, as an independent sensor, confirmed this offset.

When we compared the measurements from the optical and electrostatic sensors, using the definition of the o_{12} signal in Eq. (4), we could conclude that the measured phase of the X12 interferometer, x_{12}, corresponds to the TM positions as $x_{12} = x_{TM1} - x_{TM2}$. While this is an interesting conclusion, it is insignificant for the sensor's noise performance.

Unfortunately, the evidence of how the DOPD changed with a TM offset is not as compelling as we aimed for. However, due to the long duration of the experiment and the limited mission lifetime, it was impossible to execute the experiment again, perhaps with an even larger modulation amplitudes at the offset position.

Let us proceed to the results of the DOPD amplitude experiment, as shown in Fig. 6. As expected, we find the DOPD to be independent of the laser frequency modulation amplitude and frequency.

To analyze the evolution of Δs_{o12} and Δs_{o1} over the course of the mission, we combined the results from the two previously discussed experiments which were optimized for DOPD estimation with DOPDs estimated from the laser frequency modulations optimized for the control loop characterization. However, when using the modulations that were designed to characterize the frequency stabilization loop, it was not possible to estimate the DOPD Δs_{o1}.
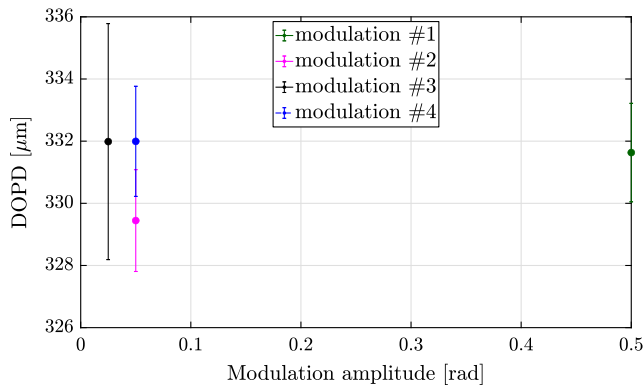

FIG. 6. The DOPD estimate Δs_{o12} for different amplitudes of the laser frequency modulation and two modulation frequencies. Note that we performed this experiment several months after the offset experiment. The evolution of the DOPD is discussed in the text. Based on [19].

We calculated the weighted mean of the results from the modulations at different frequencies and with different amplitudes to obtain a single value per experiment. There were, however, two exceptions. From the DOPD offset experiment, we included only the first two modulations at the nominal position. That was because during the other modulations, TM 2 was deliberately at an offset position, so the DOPD was intentionally changed at these times. Then, to estimate Δs_{o1} from the DOPD amplitude experiment, we could only use data from modulations 1, 2, and 4 here because the amplitude in the third modulation was too small to produce a signal in o_1.

We collected the results in Table I. The result for Δs_{o12} from 01-06-2016 was already used in [6,7] and the result for Δs_{o12} of the DOPD amplitude experiment in [7]. Throughout this document and in this Table, we correctly propagated the 1 mm uncertainty on the intentional OPD in the XF interferometer. This leads to a slight increase in the estimated uncertainty of Δs_{o12} on 13-06-2016 and 22-01-2017 from 0.8 µm (see Ref. [19]) to 1 and 0.9 µm, respectively. We find that all values are below the experimentally determined upper limit of 400 µm [20]. When we compare the Δs_{o12} measurements on 01-06-2016 and 13-06-2016, we find an agreement on the 3σ level. This is largely due to the relatively large uncertainty of Δs_{o12} on 01-06-2016, which stems from a much shorter measurement duration than the other experiments. A 17 µm change in DOPD would be unexpected and would correspond to a TM offset of approximately 8.5 µm. Such a change is not observed when the true test mass position during this time span is estimated [19].

Moreover, we identify a change in DOPD between the measurements on June 13th and 14th, 2016, and those in January 2017 of approximately 20 µm. To understand this change, note that the DOPD in the X1 and X12 interferometers depended not only on the integration but also on the absolute positions of one or both TMs, respectively. Indeed, the observed change in DOPD could be attributed to an accidentally commanded offset on TM 1 of 11.7 µm toward the center of the satellite. The data which supports this statement is shown in Fig. 7. In this figure, the electrostatic measurement of the position of TM 1 is called GRS x1. During the period shown in this figure, the satellite

TABLE I. The estimated DOPD from all laser frequency modulation experiments with free-falling test masses. We note comparable changes in Δs_{o12} and Δs_{o1} in the course of the mission due to a commanded offset on TM 1.

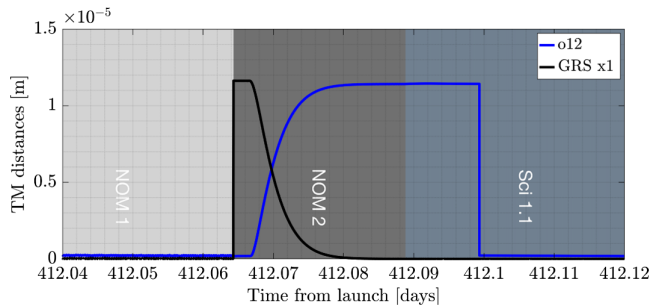| Date	Experiment	Δs_{o12} (µm)	Δs_{o1} (µm)
01-06-2016	Loop characterization	368 ± 5	$\cdots$
13-06-2016	Loop characterization	351 ± 1	$\cdots$
14-06-2016	DOPD offset	352 ± 1	148 ± 4
22-01-2017	DOPD amplitudes	329.6 ± 0.9	130 ± 1
22-01-2017	Loop characterization	330.7 ± 0.9	$\cdots$

FIG. 7. The o_{12} measurement of the OMS and the electrostatic measurement of the TM 1 position at the time of a mode transition in January 2017. Due to a wrong offset, TM1 moved by 11.7 μm, which is the main reason for the observed change in DOPD in Table I. Please refer to the main text for details. Based on [19].

is in three different control modes called NOM 1, NOM 2, and Sci 1.1. These intermediate control modes are used to transition from a satellite station-keeping period back to the nominal science configuration. At the time, the offset was commanded, it looked for the electrostatic measurement system as if TM 1 had changed its position. This is seen by the sharp increase of the black trace at the transition from NOM 1 to NOM 2. The control system forced this TM back into its nominal position around 0. In this satellite control mode, the OMS was not used to control the satellite. It was therefore acting as an out-of-loop sensor and noted the corresponding change in o_{12} since one of the two TMs was moved. This is seen by the increase of the blue trace during the time spent in NOM 2. After the satellite did the next step toward its nominal science configuration, the transition to Sci 1.1, the X12 interferometer measurement was reset as part of the routine satellite operations. This reset corresponds to the edge in the blue trace shortly before 412.1. This, however, implied that we measure the same o_{12} value as before, but the absolute distance between the two TMs was changed. This change in position led to approximately twice the change in optical path length because the measurement beam travels to each TM and is reflected on the surface, see Fig. 2. This is consistent with the observed change in amplitude and direction in DOPD at the 2σ level. In addition, the motion of TM 1 explains comparable changes in Δs_{o12} and Δs_{o1}. Even though this TM motion is the main reason for the measured changes in DOPD, one can also argue that hardware drifts may be present but on a much smaller level.

D. Additional observations

Experimental observations revealed a spurious coupling from a laser frequency modulation to the DWS measurements. For example, a laser frequency modulation of (32.4 ± 0.1) mrad resulted in a DWS measurement of (16 ± 8) $\mu\text{rad}_{\text{el}}$ against a noise floor of approximately 1.3 $\mu\text{rad}_{\text{el}}\,\text{Hz}^{-1/2}$. We use the unit rad_{el} which refers to

DWS optical phase measurements before they were calibrated to TM angles. For the calibration value, we refer to [7]. This observation was not expected. From calculation, simulation, and especially its spurious nature, we can exclude it is due to a OPD between the left and the right or the upper and the lower part of the photodiode. We reproduced and investigated a similar spurious signal in a laboratory setup. However, a definite answer could not be found [19]. On the other hand, we have found no reason to believe this could be an indication of a mechanism that impacts the longitudinal measurements, and therefore, this observation did not lead to a systematic error to the DOPD numbers reported.

When studying the two DOPD experiments further, we could observe changes in DOPD during most of the individual laser frequency modulations of the DOPD experiments. The amplitude of these fluctuations differed but was mostly on the order of a few tens of μm. Their origin is not fully understood, but mechanical path length changes or real TM motion with such amplitudes are deemed highly unlikely.

First, mechanical path length changes are very improbable because the OB was fixed to the side slabs, which in turn were fixed to the vacuum chambers, see, *e.g.*, Fig. 1 in [25]. The OB itself was also highly stable since it was made from Expansion Class 0 Zerodur and all components were bonded onto it [20]. Moreover, the TM positions were measured via electrostatic sensing and controlled via a drag-free attitude control system [4,15]. Therefore, also a change in TM positions would have been noticed.

It is worth mentioning that these short-term fluctuations in DOPD could not be seen during the strongest laser frequency modulation period. An effect, which was perhaps similar, was noticed while the laser was frequency modulated and the test masses were grabbed on April 06, 2017.

V. CHARACTERIZING THE LASER FREQUENCY STABILIZATION CONTROL LOOP ON LPF

A. Description of experiments optimized for loop characterization

We injected sinusoidal test signals into the closed-loop system to characterize the laser frequency control loop in-flight. This allowed us to estimate the transfer function of both controllers individually, as well as the response of the actuators and the combined loop response. This experiment was repeated five times throughout the mission. In each experiment, we aimed to inject 6–8 test signals at frequencies from 0.011 to 1.123 Hz with an amplitude of 6.2 MHz. The experiments were executed as planned except for experiment 2, where only a single laser frequency modulation at 0.011 Hz could be applied. We recorded 20 cycles of each modulation.

B. The measured open-loop transfer function

At first, the experimental data were corrected for small timing errors caused by the different data processing routes on board LPF. Let us summarize the detailed description from [19,26] here: The OMS data on LPF were either part of the science or the housekeeping data, and the respective data processing routes implied a different downsampling and priority. Comparing data from these two routes is a challenge specific to the analysis of the OMS loop characterization experiments. While the housekeeping data was directly downsampled in the DMU (see Fig. 1) from 100 Hz to 1 Hz, the science data was downsampled from 100 Hz to 10 Hz. Due to the different clocks on the satellite, specifically the DMU clock and the onboard computer clock, the time between two 10 Hz data samples can be offset by 10 ms. Moreover, perhaps due to the different priorities, there can be a small, time-dependent offset between the two data routes. Our approach uses that we obtain Ψ_F at 10 Hz, timestamped according to the DMU time, and the fast frequency controller error signal ff_{err} (see Fig. 3) at 1 Hz, timestamped according to the OBC time. Since the ff_{err} corresponds to the Ψ_F with the inverted sign, we can downsample the 10 Hz Ψ_F data to 1 Hz using a time offset. The best offset for each experiment was the one that maximized the correlation between data from the two routes and resulted in a flat phase of the respective transfer function up to the Nyquist frequency. We thus obtained one offset for each experiment, which varied between 0.6 and 1.7 s.

We calculated the transfer function from the timing-corrected data for each modulation using a Hanning window. The transfer function estimation provides an error based on the coherence of the signals as outlined in [24]. We show the measured open-loop transfer functions of the experiments in Fig. 8. The unity gain frequency is read off to be 0.8 Hz and the phase margin 77°. Considering the

read-off accuracy, these results agree well with the results from the so-called flight model ground test campaign [27]. The gain margin was estimated from the loop model to be approximately 19 dB. As expected, the performance of the control loop was stable over the mission and operated as expected from the ground tests. During the LPF mission, we observed reoccurring periods of increased laser frequency noise, after which the noise level decreased again. In other words, we experienced a bi-modal behavior with an upper and a lower regime [6,7,19]. The difference was approximately a factor of 1.6–2, but most of the time, the laser frequency fluctuations were in the lower regime, from 23–38 kHz/$\sqrt{Hz}$ in the frequency range from 0.2–0.5 Hz. The transition from one level to the other was a quick change within less than one minute, and no drift was observed. Most of the periods when the laser was more noisy lasted between 0 and 10 hrs. A similar behavior was already observed in test campaigns before launch. Since the laser frequency stabilization worked as expected, we conclude that the two regimes of laser frequency noise are unlikely to originate from the laser frequency control loop.

To find the origin of the bimodal behavior, we investigated several hypotheses [19]. One of these was aliasing in the downsampling from 100 to 10 Hz in the DMU. However, when we compared the rare measurements recorded at a sampling frequency of 100 Hz to the 10 Hz data, we found the measurements to agree well. In addition, the 100 Hz data was flat above 20 Hz in all measurements, which makes aliasing even more unlikely. In addition to the aliasing hypothesis, we also assumed that the level of laser frequency noise could originate in the laser itself. Therefore, we searched for correlations between the level of laser frequency noise and the laser temperature, pump current, and output power. We could observe the difference between the two levels decreasing with increasing laser temperature, but the two levels were present at all temperatures. The output power and the pump current seemed to have no effect. Moreover, we checked whether the satellite temperature, as measured on the OB, could impact the bimodal behavior. This check allowed us to exclude a linear dependency. We also checked whether, for certain TM angles, a fraction of the light on the OB is back-scattered into the laser and thus increases the laser frequency noise level. Therefore, we used data from an experiment during which one TM has been systematically tilted as well as standard LPF science measurements to check for a large range of angles. However, it is not possible to identify an orientation of either TM with increased laser frequency noise. This concludes our list of possible checks with the available data from LPF. Another possible reason for the bi-modal behavior that we cannot exclude with the data available from LPF are different modes in the pump diode. For this investigation, a flight-spare laser would need to be
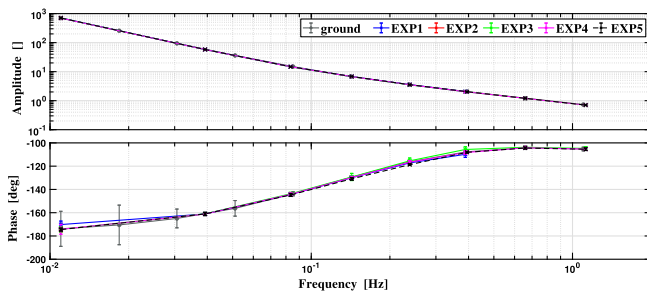

FIG. 8.   The open-loop transfer function estimates from the five characterization experiments performed during the mission (denoted as EXP1-EXP5 in the legend) compared to the control-loop model from the ground test (denoted as "ground" in the legend). We mark the results of the in-flight experiments with a cross and the ground test results with a dot at each modulation frequency, respectively. Note that the modulation frequencies were different between ground and in-flight measurements. Reprint from [19].
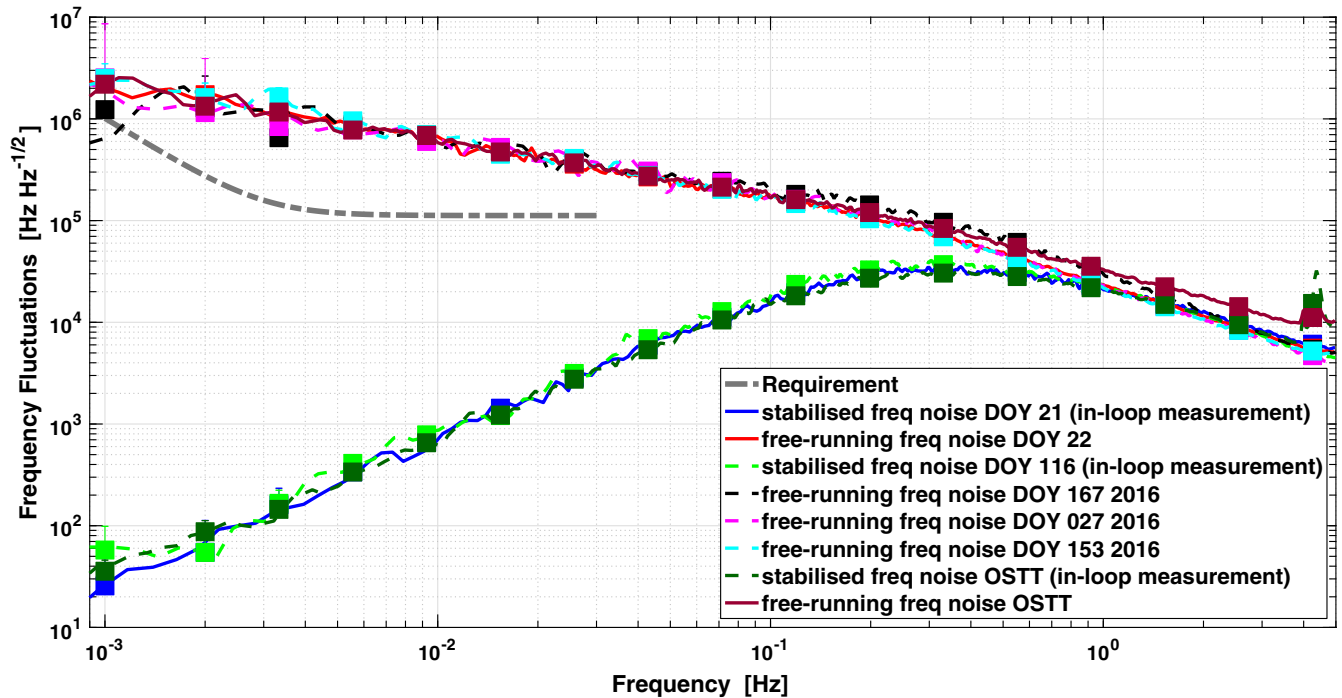
FIG. 9.   Amplitude spectral density of the laser frequency fluctuations in-flight with and without active stabilization compared to the requirement (grey dashed trace) and the last ground measurements before launch, denoted OSTT. For spectral estimation, we used a modified version of Welch's periodogram [28] with a Blackman-Harris window for the lines; the squares are estimated as in the supplemental material of [5], implemented in LTPDA [22]. The ground measurements' data quality was improved as outlined in [27]. Based on [19].

integrated into an experimental setup again. In summary, despite several investigations, the cause of the bi-modal behavior could not be identified.

C. Measurements of stabilized and free-running laser frequency noise

The performance of the laser frequency stabilization from 1 mHz to 5 Hz is shown in Fig. 9. We compare the measurements from ground testing to the four free-running measurements taken in-flight and two selected measurements of the stabilized laser frequency noise.

Note that the measurements of the stabilized laser frequency noise are in-loop measurements. Unfortunately, no out-of-loop sensor for the laser frequency fluctuations on LPF existed. Let us look at the potential implications: First, with this laser frequency stabilization setup, the control loop cannot distinguish between changes in the intentional OPD of the XF interferometer and laser frequency fluctuations. In other words, under the assumption of a perfect locking onto the reference, the frequency stability of the reference itself becomes limiting. However, we expect not to observe this with LPF. Indeed, the XF interferometer consists of bonded components onto an ultrastable OB, so even the upper limit of the thermally driven optical path length changes on the OB is below 20 pm in the frequency range of interest [6], so many orders of magnitude below the uncertainty of the intentional OPD

in the XF interferometer. Second, due to the lack of an out-of-loop sensor, we cannot rule out that, at low frequencies, sensing noise could lead to additional laser frequency fluctuations. However, our investigations of the o_{12} sensing noise revealed a phasemeter noise in o_{12} of 28.7 fm/$\sqrt{\text{Hz}}$ [6] which, following Eq. (4) and dividing by $\sqrt{2}$ under the assumption of uncorrelated noise in the X12 and XR interferometer, corresponds to ≈0.2 μrad in a single interferometer. Our evidence suggests that the phasemeter noise on LPF was white [7], so we can use this number at all frequencies. We insert this into Eq. (3) to find that we should be able to measure laser frequency fluctuations down to ≈30 Hz with this setup. This implies that the sensing noise is likely to affect only the lowest data points around 1 mHz but is not limiting for most of the frequency range shown in Fig. 9. Note that the OPD in the frequency interferometer could also be increased to overcome such a limitation if it were necessary.

The measured residual laser frequency fluctuations when the laser was stabilized could also be further reduced by increasing the gain of the laser frequency control loop by a factor 4.3 [19]. With such an increase, the loop is still expected to be stable, but the margin would be reduced to a gain margin of 2.02 in magnitude and a phase margin of 45.7°.

The selected measurements are representative of the in-flight behavior for the high-frequency range, as can be seen

by comparison to [7]. When the mission was designed, the laser frequency fluctuations were required to be below $112 \text{ kHz}/\sqrt{\text{Hz}}$ at 10 mHz with a relaxation toward the lower frequencies of the LPF measurement band from 1 to 30 mHz [27]. This requirement resulted from the aim of limiting the contribution of laser frequency noise to the total noise in o_{12} to below 2 pm at 10 mHz under the rather pessimistic assumption of a DOPD of up to 1 cm [19,21,27]. Our in-loop measurements fulfill this requirement with ample margin. Indeed, at 10 mHz, we are more than a factor 100 below this level. We can also observe that the in-flight measurements approximately agree with each other, even though some were taken with more than six months between them. The agreement between the data taken on-ground and in-flight, except for the frequency range from 1 to 4 mHz, shows that the ground tests represent the in-flight behavior.

D. From LPF to LISA

The impact of laser frequency noise in the technology demonstrator mission LPF cannot be directly transferred to the future gravitational wave observatory LISA. In LPF, this noise source contributed to the sensing noise of a key subsystem, the interferometric TM readout.

In LISA, on the other hand, the interferometric setup on different satellites results in differences between two interferometer arms of around 30 000 km [29], which will make laser frequency noise the dominant noise source by several orders of magnitude. Therefore, laser frequency noise must be suppressed in postprocessing to enable gravitational wave astrophysics. The baseline algorithm to do this is called time delay interferometry (TDI) [30,31]. However, due to, for example, variations in the distance between the two satellites and imperfect knowledge of these, we expect residual laser frequency noise after the application of TDI. This residual noise must be small enough to allow for the required measurement accuracy of the displacement between two TMs on different satellites [32]

$$S_{\text{disp}}^{1/2,\text{req}}(f) = 13.5 \frac{\text{pm}}{\sqrt{\text{Hz}}} \sqrt{1 + \left(\frac{2 \text{ mHz}}{f}\right)^4}, \quad (21)$$

for frequencies f in the LISA measurement bandwidth from 0.1 mHz–1 Hz. Therefore, the frequency fluctuations of the lasers for LISA need to be remain below

$$S_{\delta f \text{LISA}}^{1/2,\text{req}} = 30 \frac{\text{Hz}}{\sqrt{\text{Hz}}} \sqrt{1 + \left(\frac{2 \text{ mHz}}{f}\right)^4}, \quad (22)$$

which amounts to ≈ 30 Hz at 10 mHz [29,31,33].

Stabilizing the lasers to this level will be difficult using only the frequency stabilization approach as on LPF. In Fig. 9, we found the in-loop laser frequency fluctuations on LPF to be around 600–900 kHz at 10 mHz. So, we must measure significantly smaller laser frequency fluctuations on LISA than on LPF. However, we expect larger phasemeter noise on LISA than on LPF. To be more precise, we expect $\approx 6 \text{ μrad}/\sqrt{\text{Hz}}$ for LISA (see Ref. [34]). With LPF, we reached a phasemeter noise in o_{12} of $28.7 \text{ fm}/\sqrt{\text{Hz}}$ [6] which corresponds to ≈ 0.2 μrad in a single interferometer, so approximately a factor 30 less. The phasemeters on LISA and LPF differ in many ways, for example, in the readout frequencies, the number of channels, and the phase extraction algorithms used. A detailed comparison is beyond the scope of this paper. Consequently, if we wanted to stabilize the laser on LISA with the same approach as on LPF, this would require a huge amplification via the intentional OPD in a frequency interferometer on LISA. Following Eq. (3), this OPD would need to be

$$\Delta s = \frac{c}{2\pi} \frac{\Delta\tilde{\varphi}}{\delta\tilde{f}} \approx 10 \text{ m}. \quad (23)$$

This is significantly larger than on LPF and impractical to accommodate on an OB with roughly 50 cm diameter. Moving the OPD into the fibers which lead to the OB, however, also implies that this OPD needs to be compensated in the other interferometers on the OB and thus does not solve the issue but moves it to the other interferometers.

In the past, the technique presented here was suggested as a candidate for prestabilization, to be combined with locking to the LISA arms [1]. However, a cavity as a frequency reference does fulfill the LISA requirements as demonstrated in laboratory tests and, therefore was considered mature technology at the time of the mission proposal [2]. In the meantime, the laser frequency stabilization to a cavity was successfully used on the laser ranging instrument on the GRACE Follow-On mission [35]. In summary, the laser frequency stabilization on LISA will not be implemented like on LPF, but a cavity like on the GRACE Follow-On mission will be used. To be more precise, this will only apply to one of the six lasers on LISA, the primary laser. The other five lasers will be transponder-locked to the primary laser; see Sec. VI in [36].

VI. CONCLUSIONS

LISA Pathfinder (LPF) was a satellite mission to demonstrate the technology for the future space-borne gravitational wave observatory LISA. A high-precision interferometric readout system was a key part of this payload. It performed significantly better in flight than in the preceding ground tests [7]. This turned laser frequency noise into one of the limiting noise sources [6,7]. Under nominal conditions, this noise contribution amounted to $(22 \pm 1) \text{ fm}/\sqrt{\text{Hz}}$ [6]. During periods of increased laser frequency, we measured $\approx 38 \text{ fm}/\sqrt{\text{Hz}}$, see Fig. 14 in [7]. This paper reported on how this noise source was suppressed during the LPF mission.

On LPF, the laser was frequency stabilized by the following scheme: the laser frequency fluctuations were measured by a dedicated interferometer with an intentional OPD and suppressed via a control loop. This approach was tested before on the ground [27,37], as well as a similar approach using balanced homodyne DC readout [38,39]. Compared to laser frequency stabilization using a cavity, this approach can help to save space on a satellite and works for a large range of laser frequencies, which can be useful during signal acquisition, see Ref. [40]. This comes at the cost of increased complexity by another interferometer on the OB and does not allow for independent testing of the laser and the OB unit. We found that this laser frequency stabilization scheme worked reliably during the LPF mission and kept the laser frequency fluctuations below the required level throughout the entire mission. The performance of the control loop agreed with expectations from ground tests. This allows us to conclude that the bimodal behavior of the laser frequency fluctuations throughout the mission is unlikely to originate from the laser frequency control loop. Therefore, this approach would be applicable to other experiments and space missions which require laser frequency fluctuations to be limited to a few 100 Hz level at mHz frequencies. Moreover, the performance could be further improved by an increase in the fast actuator gain. Another option would be to increase the deliberate OPD in the frequency interferometer if the sensing noise limit was reached.

The coupling of the laser frequency fluctuations into the phase measurement on LPF was proportional to the DOPD. Consequently, this number was minimized during the design and construction of LPF. In-flight, the DOPD was measured several times during the mission and was found to vary between (368 ± 5) μm and (329.6 ± 0.9) μm. In an early stage of the mission development, a worst-case DOPD of up to 1 cm was assumed [21]. Later, the DOPD requirement was set to 1 mm [20]. All measured values are significantly below this number. On-ground, an experimental upper limit of 400 μm was deduced [20], which is consistent with the in-flight measurements. However, the actual position of the TMs influences this number. During ground testing, the TMs had to be replaced with mirrors that were put at the expected location of the TMs. Any difference between their expected and actual locations would lead to a difference in DOPD. Nonetheless, the small DOPD in o_1 and o_{12} measured in-flight confirmed the excellent construction and assembly of the OB and its integration into the satellite, as well as the stability of the system through launch and transfer. In addition, we saw that the DOPD estimate can be a useful tool to monitor the changes in the absolute TM positions. Even though we could not resolve all the questions that arose during the detailed analysis of the dedicated experiments, we have found no reason to believe that those observations could indicate a mechanism that adds a systematic error to the DOPD numbers reported.

The combination of the laser frequency stabilization and the path length matching achieved thus made the high precision measurements of the LPF interferometric readout system possible. Indeed, this system achieved a total sensing noise of only $32.0^{+2.4}_{-1.7}$ fm/$\sqrt{\text{Hz}}$ above 200 mHz [6,7]. The analysis presented in this article shows that we achieved a detailed understanding of the laser frequency noise and its impact on the LPF interferometry. This is not only making the best use of unique data but also increases the confidence in our noise model, as shown in [6,7].

[1] LISA Science Team, LISA—Unveiling a hidden Universe, Technical Report, 2011, also available as http://sci.esa.int/science-e/www/object/doc.cfm?fobjectid=48363.

[2] P. Amaro-Seoane *et al.*, Laser interferometer space antenna, arXiv:1702.00786.

[3] P. Amaro-Seoane *et al.*, Astrophysics with the Laser Interferometer Space Antenna, Living Rev. Relativity **26**, 2 (2023).

[4] M. Armano *et al.*, Sub-Femto-g free fall for space-based gravitational wave observatories: LISA pathfinder results, Phys. Rev. Lett. **116**, 231101 (2016).

[5] M. Armano *et al.*, Beyond the required LISA free-fall performance: New LISA pathfinder results down to 20 μHz, Phys. Rev. Lett. **120**, 061101 (2018).

[6] M. Armano *et al.*, Sensor noise in LISA pathfinder: In-flight performance of the optical test mass readout, Phys. Rev. Lett. **126**, 131103 (2021).

[7] M. Armano *et al.*, Sensor noise in LISA Pathfinder: An extensive in-flight review of the angular and longitudinal interferometric measurement system, Phys. Rev. D **106**, 082001 (2022).

[8] H. Billing, K. Maischberger, A. Rudiger, R. Schilling, L. Schnupp, and W. Winkler, An argon laser interferometer for the detection of gravitational radiation, J. Phys. E **12**, 1043 (1979).

[9] D. Robertson, C. Killow, H. Ward, J. Hough, G. Heinzel, A. Garcia, V. Wand, U. Johann, and C. Braxmaier, LTP interferometer-noise sources and performance, Classical Quantum Gravity **22**, S155 (2005).

[10] G. Heinzel, C. Braxmaier, R. Schilling, A. Rüdiger, D. Robertson, M. te Plate, V. Wand, K. Arai, U. Johann, and K. Danzmann, Interferometry for the LISA technology package (LTP) aboard SMART-2, Classical Quantum Gravity **20**, S153 (2003).

[11] G. Heinzel, V. Wand, A. García, O. Jennrich, C. Braxmaier, D. Robertson, K. Middleton, D. Hoyland, A. Rüdiger, R. Schilling, U. Johann, and K. Danzmann, The LTP interferometer and phasemeter, Classical Quantum Gravity **21**, S581 (2004).

[12] H. Audley *et al.*, The LISA pathfinder interferometry—hardware and system testing, Classical Quantum Gravity **28**, 094003 (2011).

[13] E. Morrison, B. J. Meers, D. I. Robertson, and H. Ward, Automatic alignment of optical interferometers, Appl. Opt. **33**, 5041 (1994).

[14] D. Robertson, 3OB as built OptoCAD model—S2-UGL-TN-3045, Technical Report, University of Glasgow, 2013.

[15] A. Schleicher, T. Ziegler, R. Schubert, N. Brandt, P. Bergner, U. Johann, W. Fichter, and J. Grzymisch, In-orbit performance of the LISA Pathfinder drag-free and attitude control system, CEAS Space J. **10**, 471 (2018).

[16] M. Armano *et al.*, LISA pathfinder platform stability and drag-free performance, Phys. Rev. D **99**, 082001 (2019).

[17] M. Armano *et al.*, Capacitive sensing of test mass motion with nanometer precision over millimeter-wide sensing gaps for space-borne gravitational reference sensors, Phys. Rev. D **96**, 062004 (2017).

[18] Sarah Paczkowski (on behalf of the LPF Collaboration), Laser frequency noise stabilisation and interferometer path

[19] length differences on LISA pathfinder, J. Phys. Conf. Ser. **840**, 012004 (2017).

[19] S. Paczkowski, Laser frequency stabilisation and interferometer path length differences during the LISA pathfinder satellite mission, Ph.D. thesis, Leibniz Universität Hannover, 2021, 10.15488/11130.

[20] D. I. Robertson, E. D. Fitzsimons, C. J. Killow, M. Perreur-Lloyd, H. Ward, J. Bryant, A. M. Cruise, G. Dixon, D. Hoyland, D. Smith, and J. Bogenstahl, Construction and testing of the optical bench for LISA pathfinder, Classical Quantum Gravity **30**, 085006 (2013).

[21] M. Kersten, OMS-control loop stability analysis and filter design—S2-ASD-TN-3107, Technical Report, Astrium, 2011.

[22] M. Hewitson *et al.*, Data analysis for the LISA Technology Package, Classical Quantum Gravity **26**, 094003 (2009).

[23] J. S. Bendat and A. G. Piersol, *Engineering Applications of Correlation and Spectral Analysis* (Wiley, New York, 1980).

[24] M. Nofrarias, F. Gibert, N. Karnesis, A. F. García, M. Hewitson, G. Heinzel, and K. Danzmann, Subtraction of temperature induced phase noise in the LISA frequency band, Phys. Rev. D **87**, 102003 (2013).

[25] F. Gibert *et al.*, Thermo-elastic induced phase noise in the LISA Pathfinder spacecraft, Classical Quantum Gravity **32**, 045014 (2015).

[26] K. Danzmann *et al.*, LPF final report for the German contribution to the nominal mission, Technical Report, AEI, 2018, 10.2314/GBV:1030758840.

[27] H. Audley, Preparing for LISA pathfinder operations: Characterisation of the optical metrology system, Ph.D. thesis, Leibniz Universität Hannover, 2014, 10.15488/8220.

[28] M. Tröbs and G. Heinzel, Improved spectrum estimation from digitized time series on a logarithmic frequency axis, Measurement **39**, 120 (2006).

[29] O. Hartwig, Instrumental modelling and noise reduction algorithms for the Laser Interferometer Space Antenna, Ph.D. thesis, Leibniz Universität Hannover, 2021, 10.15488/11372.

[30] O. Hartwig, J.-B. Bayle, M. Staab, A. Hees, M. Lilley, and P. Wolf, Time-delay interferometry without clock synchronization, Phys. Rev. D **105**, 122008 (2022).

[31] J.-B. Bayle, O. Hartwig, and M. Staab, Adapting time-delay interferometry for LISA data in frequency, Phys. Rev. D **104**, 023006 (2021).

[32] S. Paczkowski, R. Giusteri, M. Hewitson, N. Karnesis, E. D. Fitzsimons, G. Wanner, and G. Heinzel, Postprocessing subtraction of tilt-to-length noise in LISA, Phys. Rev. D **106**, 042005 (2022).

[33] G. Mueller, P. McNamara, I. Thorpe, and J. Camp, Laser frequency stabilization for LISA, Technical Report, NASA, 2005, https://ntrs.nasa.gov/api/citations/20060012084/downloads/20060012084.pdf.

[34] T. Schwarze, Phase extraction for laser interferometry in space: Phase readout schemes and optical testing, Ph.D. thesis, Leibniz Universität Hannover, 2018, 10.15488/4233.

[35] K. Abich *et al.*, In-orbit performance of the GRACE follow-on laser ranging interferometer, Phys. Rev. Lett. **123**, 031101 (2019).

[36] J.-B. Bayle and O. Hartwig, Unified model for the LISA measurements and instrument simulations, Phys. Rev. D **107**, 083019 (2023).

[37] G. Hechenblaikner, V. Wand, M. Kersten, K. Danzmann, A. García, G. Heinzel, M. Nofrarias, and F. Steier, Digital laser frequency control and phase-stabilization loops in a high precision space-borne metrology system, IEEE J. Quantum Electron. **47**, 651 (2011).

[38] O. Gerberding, K.-S. Isleif, M. Mehmet, K. Danzmann, and G. Heinzel, Laser-frequency stabilization via a quasimono-lithic Mach-Zehnder interferometer with arms of unequal length and balanced dc readout, Phys. Rev. Appl. **7**, 024027 (2017).

[39] V. Huarcaya, M. D. Álvarez, D. Penkert, S. Gozzo, P. M. Cano, K. Yamamoto, J. J. E. Delgado, M. Mehmet, K. Danzmann, and G. Heinzel, 2×10^{-13} Fractional laser-frequency stability with a 7-cm unequal-arm Mach-Zehnder interferometer, Phys. Rev. Appl. **20**, 024078 (2023).

[40] B. Sheard, G. Heinzel, and K. Danzmann, LISA long-arm interferometry: An alternative frequency pre-stabilization system, Classical Quantum Gravity **27**, 084011 (2010).